1

2 **Title: Monitoring land surface albedo and vegetation dynamics using high spatial**

3 **and temporal resolution synthetic time series from Landsat and the MODIS**

4 **BRDF/NBAR/albedo product**

5

6

7 **Authors:** Zhuosen Wang[1,3*], Crystal B. Schaaf[2], Qingsong Sun[2], JiHyun Kim[4], Angela M. Erb[2],

8 Feng Gao[5], Miguel O. Román[3], Yun Yang[5], Shelley Petroy[6], Jeffrey R. Taylor[7], Jeffrey G.

9 Masek[3], Jeffrey T. Morisette[8], Xiaoyang Zhang[9], Shirley A. Papuga[10]

10

11 **Affiliations:**

12

13 [1]Earth System Science Interdisciplinary Center, University of Maryland College Park, College Park, MD, USA

14

15 [2]School for the Environment, University of Massachusetts Boston, Boston, MA, USA.

16

17 [3]NASA Goddard Space Flight Center, Greenbelt, MD, USA.

18

19 [4]Department of Geography, Indiana University Bloomington, Bloomington, IN, USA.

20

21 [5] USDA, Agricultural Research Service, Hydrology and Remote Sensing Laboratory, Beltsville, MD, USA

22

23 [6]National Ecological Observatory Network, Boulder, CO, USA.

24

25 [7]Institute of Technology Campus, Nova Scotia Community College, Halifax, NS, Canada

26

27 [8]U.S. Geological Survey, Department of the Interior North Central Climate Science Center, Fort Collins, CO, USA

28

29 [9]Geospatial Sciences Center of Excellence, South Dakota State University, Brookings, SD, USA.

30

31 [10]School of Natural Resources and the Environment, University of Arizona, Tucson, Arizona, USA.

32

33 *Correspondence to: zhuosen.wang@nasa.gov

34

35

36 Key words: Albedo; Vegetation Index; Data Fusion; Phenology; Remote sensing

37

38

39 Key points:

40

41 1. Synthetic time series of albedo and EVI can capture land surface dynamics with high
42 similarity to tower and field data.

43 2. The RMSE and bias of the synthetic albedo values are less than 0.013 and within $\pm$ 0.006,
44 respectively as compared to Ameiflux field data

45 3. In the future access to spatially representative NEON tower albedometer data will greatly
46 improve our ability to evaluate moderate resolution satellite products.

47
48
49

1

50  **Abstract:**

51

52  Seasonal vegetation phenology can significantly alter surface albedo which in turn affects the

53  global energy balance and the albedo warming/cooling feedbacks that impact climate change. To

54  monitor and quantify the surface dynamics of heterogeneous landscapes, high temporal and

55  spatial resolution synthetic time series of albedo and the enhanced vegetation index (EVI) were

56  generated from the 500 m Moderate Resolution Imaging Spectroradiometer (MODIS)

57  operational Collection V006 daily BRDF/NBAR/albedo products and 30 m Landsat 5 albedo and

58  near-nadir reflectance data through the use of the Spatial and Temporal Adaptive Reflectance

59  Fusion Model (STARFM). The traditional Landsat Albedo (Shuai et al., 2011) makes use of the

60  MODIS BRDF/Albedo products (MCD43) by assigning appropriate BRDFs from coincident

61  MODIS products to each Landsat image to generate a 30 m Landsat albedo product for that

62  acquisition date. The available cloud free Landsat 5 albedos (due to clouds, generated every 16

63  days at best) were used in conjunction with the daily MODIS albedos to determine the

64  appropriate 30 m albedos for the intervening daily time steps in this study. These enhanced daily

65  30 m spatial resolution synthetic time series were then used to track albedo and vegetation

66  phenology dynamics over three Ameriflux tower sites (Harvard Forest in 2007, Santa Rita in

67  2011 and Walker Branch in 2005). These Ameriflux sites were chosen as they are all quite

68  nearby new towers coming on line for the National Ecological Observatory Network (NEON),

69  and thus represent locations which will be served by spatially paired albedo measures in the near

70  future. The availability of data from the NEON towers will greatly expand the sources of tower

71  albedometer data available for evaluation of satellite products. At these three Ameriflux tower

72  sites the synthetic time series of broadband shortwave albedos were evaluated using the tower

73  albedo measurements with a Root Mean Square Error (RMSE) less than 0.013 and a bias within

74  the range of $\pm 0.006$. These synthetic time series provide much greater spatial detail than the 500

75  m gridded MODIS data, especially over more heterogeneous surfaces, which improves the

76  efforts to characterize and monitor the spatial variation across species and communities. The

77  mean of the difference between maximum and minimum synthetic time series of albedo within

78  the MODIS pixels over a subset of satellite data of Harvard Forest (16 km by 14 km) was as high

79  as 0.2 during the snow-covered period and reduced to around 0.1 during the snow-free period.

80  Similarly, we have used STARFM to also couple MODIS Nadir BRDF Adjusted Reflectances

81    (NBAR) values with Landsat 5 reflectances to generate daily synthetic times series of NBAR and

82    thus Enhanced Vegetation Index (NBAR-EVI) at a 30 m resolution. While normally STARFM is

83    used with directional reflectances, the use of the view angle corrected daily MODIS NBAR

84    values will provide more consistent time series. These synthetic times series of EVI are shown to

85    capture seasonal vegetation dynamics with finer spatial and temporal details, especially over

86    heterogeneous land surfaces.

87

88    **1. Introduction**

89

90    Global surface temperatures have increased by approximately 0.6°C in the past three decades

91    (Hansen et al., 2010, 2006). This warming has contributed to a lengthening of the terrestrial

92    vegetation growing season, especially in the mid- and high latitudes (Körner and Basler, 2010;

93    Menzel and Fabian, 1999; Menzel et al., 2006; Myneni et al., 1997). Changes in the timing of

94    leaf-out impact essential ecosystem processes; therefore accurate monitoring of phenology is

95    required to understand the variability in terrestrial ecosystem change (Baldocchi et al., 2001;

96    Churkina et al., 2005; Cleland et al., 2006; Piao et al., 2007; Richardson et al., 2012, 2009).

97

98    Land surface albedo plays a crucial role in land surface climate and biosphere models as a key

99    climate forcing variable (Dirmeyer and Shukla, 1994; Hall, 2004; Lofgren, 1995; Ollinger et al.,

100   2008). Typical surface albedo can range from as high as 0.8 over a pure snow-covered area to as

101   low as 0.1 over vegetation during the snow-free period(Jin et al., 2002). This suggests that

102   climate-driven changes in phenology (e.g. the onset of spring and snowmelt) may result in

103   significant changes in the surface albedo. At lower albedo, the surface absorbs more solar energy

104   and increases the local surface temperature which in turn affects the timing of phenological

105   events (Richardson et al., 2013). This surface albedo feedback loop perpetuates further warming

106   and climate change.

107

108   Trend analysis of vegetation albedo and phenology has been previously carried out using the

109   high temporal resolution 500 m gridded MODIS albedo and Nadir Bidirectional Reflectance

110   Distribution Function (BRDF)-Adjusted Reflectance (NBAR)-derived Vegetation Indices (VI)

111   (Friedl et al., 2014; Ganguly et al., 2010; Zhang et al., 2003) ]. The MODIS 500 m

3

112  BRDF/NBAR/albedo product (MCD43A) (Schaaf, 2008; Schaaf et al., 2011, 2002) provides

113  high quality surface reflectance anisotropy retrievals over a variety of land surface types with

114  high accuracy (Jin et al., 2003; Liang et al., 2002; Liu et al., 2009; Román et al., 2010, 2009;

115  Wang et al., 2012, 2014). MODIS NBAR (MCD43A4) standardizes the MODIS directional

116  reflectances to a nadir view at the illumination of local solar noon to eliminate the angular effect

117  on the biophysical related parameters.

118

119  However, there are limitations to the application of daily 500 m gridded MODIS products such

120  as NBAR and albedo in highly heterogeneous landscapes. Snow cover over different land types

121  within a single MODIS pixel may melt at different rates and the vegetation green-up within a

122  coarse satellite pixel of a mixed land cover type is usually dominated by the proportion of

123  vegetation with the earlier green-up times (Zhang et al., 2017). As such, enhanced high

124  resolution temporal and spatial data are critical to enable more detailed phenological monitoring

125  (Liang et al., 2014). A persistent issue with current remotely sensed data is that sensors capture

126  either high spatial resolution and low temporal resolution (e.g. Landsat, ASTER) or coarser

127  spatial resolution and higher temporal resolution (e.g. MODIS, VIIRS). This limits the ability to

128  monitor rapid land surface processes, particularly in heterogeneous landscapes. Several

129  algorithms have been developed to blend these two resolutions of datasets to generate high

130  temporal and spatial resolution surface reflectance (Emelyanova et al., 2013; Gao et al., 2006;

131  Hilker et al., 2009; Roy et al., 2008; Zhu et al., 2010; Zurita-Milla et al., 2009). The Spatial and

132  Temporal Adaptive Reflectance Fusion Model (STARFM) (Gao et al., 2006) has been

133  successfully applied to generate high spatial and temporal resolution reflectance time series by

134  combining cloud-free Landsat and MODIS reflectance data for vegetation monitoring. In this

135  study, the STARFM algorithm is utilized to produce high spatial and temporal resolution albedo

136  and VI time series by fusing Landsat and MODIS data.

137

138  Essential in the development of accurate satellite-driven remotely sensed products is the need for

139  ground validation over various land covers, temporal scales, and seasonal dynamics over the

140  long-term. In order to examine the ability of long-term field and tower networks such as

141  Ameriflux and specifically the new National Ecological Observation Network (NEON) to

142  provide *in situ* reference data for MODIS and other moderate resolution satellite sensors, we

4

143  present here an analysis of the spatial representativeness of the 20 core NEON terrestrial tower

144  sites and thus their suitability to serve as moderate resolution albedo evaluation sites. NEON is a

145  comprehensive observatory network designed to monitor physical and chemical properties of

146  climate-related processes, including airborne remote sensing measurements, over the U.S.

147  continental-scale ecosystem (Kampe, 2010; Keller et al., 2008). NEON sites are designed and

148  sited to obtain accurate flux measurements, but the tower locations for other tower-based

149  measurements such as albedo are not necessarily well suited for the evaluation of coarse

150  resolution satellite acquisitions. Thus the STARFM method is used to generate synthetic high

151  resolution albedo as well as NBAR-based vegetation indices at several select Ameriflux sites that

152  are in close proximity to core NEON sites.  This is done both to further demonstrate the

153  enhancement that coupled MODIS-Landsat data products (including albedo and NBAR) provide

154  for the detection of land surface characteristics and to illustrate the value of the increasingly

155  available NEON tower data for satellite product validation over a wide range of ecosystems.

156

157  Thus the objectives of this study are to investigate the representativeness of tower measurements

158  from NEON for the validation of moderate spatial resolution albedo products (e.g. MODIS,

159  VIIRS) and demonstrate the concept of improving the ability to monitor temporal vegetation

160  variations at the landscape scale especially heterogeneous surface by using STARFM to generate

161  high temporal (daily) and spatial (30m) resolution albedo and NBAR-derived vegetation indices

162  from the Collection V006 MODIS BRDF/NBAR/albedo products and Landsat 5 data.

163

164     **2.  Material and methodology**

165     **2.1 Study area and ground measurements**

166  NEON consists of 47 terrestrial tower sites located across 20 eco-climatic domains in the US

167  with one "core site" at each domain. Each of the 20 core terrestrial sites (Fig. 1) represents a

168  different ecosystem region with varying vegetation types and climates (Hamilton et al., 2007;

169  Kampe, 2010; Schimel et al., 2007). Long-term (30 year) data acquisition from NEON will

170  provide site-based field ecological and climatic observations which can be coupled with regional

171  and national-scale airborne remote sensing observations to describe land use and climate-driven

172  seasonal change. The NEON network is currently under construction (with only nine sites

173  starting to be operational), therefore we selected three Ameriflux tower sites (Harvard Forest,

174    Santa Rita and Walker Branch) (Table 1) which are located very close to NEON sites. These

175    Ameriflux sites have the same land cover type as their NEON counterparts and the distances

176    between the NEON and Ameriflux tower pairs are less than 0.8 km in all cases. The AmeriFlux

177    network, established by the Department of Energy (DOE), provides ecosystem level exchanges

178    of $CO_2$, water, and energy (including surface albedo) (Law et al., 2002; Running et al., 1999). In

179    this study the Ameriflux tower measurements were used to evaluate the daily high spatial

180    resolution synthetic time series of albedo. The Harvard Forest site is a mixed deciduous

181    broadleaf and evergreen needleleaf forest dominated by red maple (*Acer rubrum*), red oak

182    (*Quercus rubra*), birch (*Betula*), and hemlock (*Tsuga canadensis*). The Walker Branch site is

183    near the NEON Oak Ridge site and is a 50-year-old broadleaf forest stand dominated by oak

184    (*Quercus alba L., Q. prinus L.*), hickory (*Carya ovata(Mill.) K. Koch*), maple (*Acer rubrum L.,*

185    *A. saccharum*), and tulip poplar (*Liriodendron tulipifera L.*). Both of these Ameriflux towers are

186    mounted with Kipp and Zonen albedometers and radiometers to measure shortwave albedo. The

187    Santa Rita Creosote site is located near the NEON Santa Rita Experimental Range site. This

188    open shrub site is dominated by creosote bush (*Larrea tridentata*) and the shortwave albedo is

189    derived from a Kipp and Zonen four component radiometer (Sanchez-Mejia and Papuga, 2014;

190    Sanchez-Mejia et al., 2014). The local noon ground albedo is calculated as the ratio of upwelling

191    radiation and downwelling radiation. In addition, field measurements of green-up dates with full

192    bud break were obtained at the Harvard Forest site through the long-term ecological research

193    (LTER) network database (http://www.lternet.edu/sites/hfr) (Richardson and O'Keefe, 2009;

194    Zhang et al., 2006). Phenocam photos acquired at Santa Rita Creosote site were used to track the

195    vegetation dynamics.
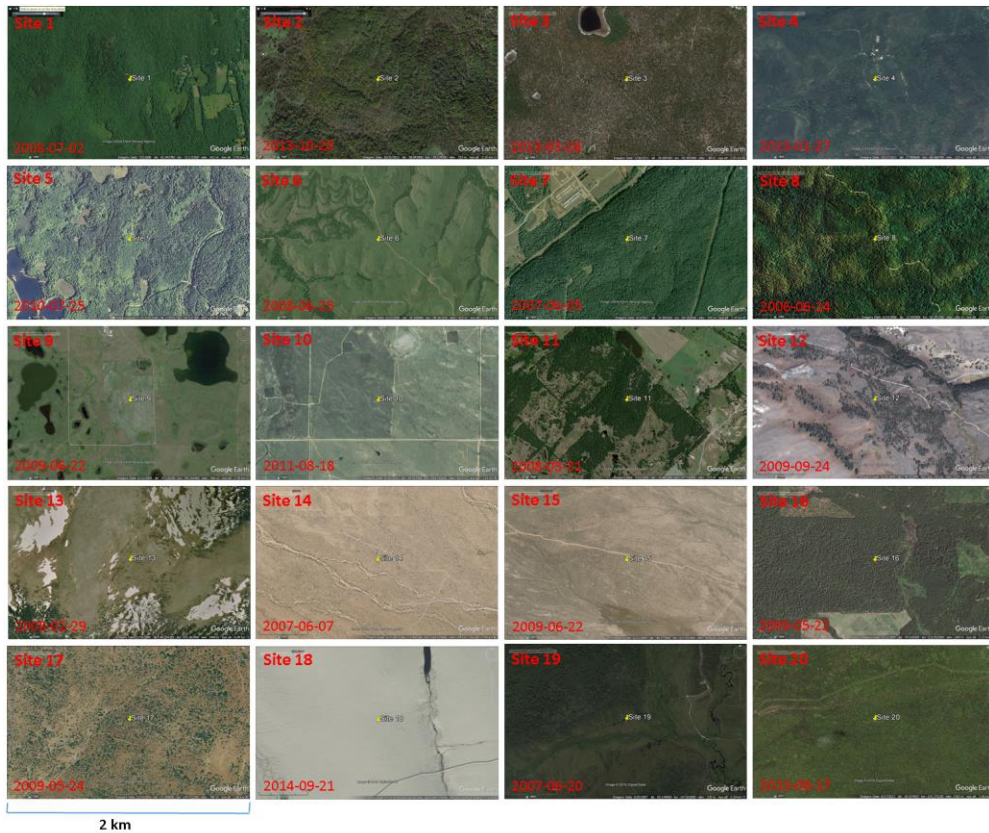
196

197 Fig. 1 Landscapes and acquired dates of the 20 NEON core sites (from Google Earth).

198

199 Table 1: Characteristics of the three Ameriflux and 20 NEON tower sites in 20 NEON domains

| Domain Number | Site Name | Network | Latitude/Longitude | State | Land type | Tower height (m) |
|---|---|---|---|---|---|---|
| D01 | Harvard Forest | NEON | 42.5369/-72.1727 | Massachusetts | Mixed Forest | 36 |
| D01 | Harvard Forest | Ameriflux | 42.54378/-72.1715 | Massachusetts | Mixed Forest | 30 |
| D02 | Smithsonian Conservation Biology Institute | NEON | 38.8929/-78.1395 | Virginia | Deciduous broadleaf forest | 50 |
| D03 | Ordway-Swisher Biological Station | NEON | 29.6893/-81.9934 | Florida | Evergreen broadleaf forest | 33 |
| D04 | Guanica Forest | NEON | 17.9696/-66.8687 | Puerto Rico | Evergreen broadleaf forest | 20 |
| D05 | University of Notre Dame Environmental | NEON | 46.2339/-89.5373 | Michigan | Mixed forest | 36 |

7

| | | | | | | |
|---|---|---|---|---|---|---|
| | Research Center | | | | | |
| D06 | Konza Prairie Biological Station | NEON | 39.1008/-96.5631 | Kansas | Prairie | 8 |
| D07 | Oak Ridge | NEON | 35.9641/-84.2826 | Tennessee | Deciduous broadleaf forest | 38 |
| D07 | Walker Branch | Ameriflux | 35.9588/-84.2874 | Tennessee | Deciduous broadleaf forest | 44 |
| D08 | Talladega National Forest | NEON | 32.9505/-87.3933 | Alabama | Mixed forest | 35 |
| D09 | Woodworth | NEON | 47.1282/-99.2414 | North Dakota | Grass | 8 |
| D10 | Central Plains Experimental Range | NEON | 40.8155/-104.7456 | Colorado | grass | 8 |
| D11 | LBJ National Grassland | NEON | 33.4012/-97.5700 | Texas | Deciduous broadleaf forest | 22 |
| D12 | Yellowstone Northern Range (Frog Rock) | NEON | 44.9535/-110.5391 | Wyoming | Evergreen needleleaf forest | 20 |
| D13 | Niwot Ridge Mountain Research Station | NEON | 40.0543/-105.5824 | Colorado | grass | 8 |
| D14 | Santa Rita Experimental Range | NEON | 31.9107/-110.8355 | Arizona | shrub | 8 |
| D14 | Santa Rita Creosote | Ameriflux | 31.9083/-110.8396 | Arizona | shrub | 2.75 |
| D15 | Onaqui-Ault | NEON | 40.1776/-112.4524 | Utah | sagebrush steppe | 8 |
| D16 | Wind River Experimental Forest | NEON | 45.8205/-121.9519 | Washington | Evergreen needleleaf forest | 86 |
| D17 | San Joaquin Experimental Range | NEON | 37.1088/-119.7323 | California | open woodland | 36 |
| D18 | Toolik Lake | NEON | 68.6611/-149.3705 | Alaska | tundra | 8 |
| D19 | Caribou Creek - Poker Flats Watershed | NEON | 65.1540/-147.5026 | Alaska | Evergreen needleleaf forest | 18 |
| D20 | Upper Waiakea Forest Reserve | NEON | 19.5577/-155.2711 | Hawaii | Evergreen broadleaf forest | 20 |

200

201    **2.2 Satellite Data**

202    The 500 m Collection V006 MODIS BRDF/NBAR/albedo product (MCD43) and the 30 m

203    Landsat 5 surface reflectance were used for this synthetic study. The MODIS

204    BRDF/NBAR/albedo product makes use of a linear "kernel-driven" RossThick-LiSparse

205    Reciprocal (RTLSR) BRDF model which has been shown to be well suited to describe the

206    reflectance anisotropy of each pixel at a 500-m gridded resolution over a variety of land covers

207    (Lucht et al., 2000; Privette et al., 1997; Schaaf et al., 2002). In the past this multi-day product

208    was retrieved every 8 days which limited its ability to capture rapidly changing land surface

209    events such as vegetation emergence and snowmelt. However, the Collection V006 MODIS

210    BRDF/albedo product, currently in production, is now retrieved daily and represents the best

211    possible BRDF based on 16 days of input information.  The day of interest is heavily weighted

212    within the algorithm to allow daily monitoring of land surface change phenomena (Schaaf et al.,

213    2011; Shuai et al., 2013; Wang et al., 2012).

214

215    The 30 m spatial resolution Landsat 5 surface reflectance over the three sites is derived from

216    Landsat Ecosystem Disturbance Adaptive Processing System (LEDAPS) (Masek et al., 2006).

217    The Landsat narrowband to broadband coefficients were applied to generate the shortwave

218    broadband surface reflectance (He et al., 2014; Shuai et al., 2014). Landsat shortwave albedo is

219    calculated from the Anisotropic Reflectance Factor (ARF) taken from a high quality MODIS

220    pixel associated with the same spectral cluster (Shuai et al., 2011; Wang et al., 2012). The Shuai

221    et al. (2011) (the so-called concurrent "MODIS-era" approach) uses an unsupervised classifier to

222    cluster the individual scene-based multi-spectral Landsat data into ten to fifteen clusters, with the

223    assumption that each cluster in the scene has similar instantaneous anisotropy features. The

224    cluster map is reprojected from UTM to the MODIS sinusoidal projection and MODIS

225    representative pixels that are relatively homogenous on the Landsat scale are identified. The ratio

226    of the albedo-to-reflectance generated from the representative MODIS pixels BRDF which are

227    associated with each Landsat cluster is then calculated to derive a Landsat albedo from the

228    Landsat near nadir reflectance (at view angles ±7.5° from nadir) using equation (1).

$$A = (a/r(\Omega_l)) \cdot r_l \qquad\qquad (1)$$

229    Where $A$ is Landsat albedo to be calculated, $r_l$ is observed Landsat reflectance and $\Omega_l$ is viewing

230    and solar geometry of Landsat data. $a$ is albedo and $r(\Omega_l)$ is the reflectance at Landsat sun view

231    geometry. Both $a$ and $r(\Omega_l)$ are derived by the BRDF parameters.

9

232

233 The cloud-free blue-sky shortwave broadband albedo (the actual bi-hemispherical reflectance) is

234 derived by combining the synthetic shortwave Black-Sky Albedo (BSA) at local solar noon and

235 the White-Sky Albedo (WSA) with a consideration of the diffuse and direct incident radiation at

236 a specific time (Eq. 2) (Lewis and Barnsley, 1994; Román et al., 2010).

237

238 $$\alpha_{blue-sky}(\theta_i) = f_{diffuse}(\theta_i)\alpha_{white-sky} + (1 - f_{diffuse}(\theta_i))\alpha_{black-sky}(\theta_i) \tag{2}$$

239

240 Where $f_{diffuse}(\theta_i)$ is the proportion of diffuse irradiation at a specific solar zenith angle $\theta_i$; the

241 $f_{diffuse}$ is derived from AOD acquired from the MODIS aerosol product (MOD08).

242

243 Compared to the Normalized Difference Vegetation Index (NDVI) which can become saturated

244 in dense vegetation, the Enhanced Vegetation Index (EVI) (Huete et al., 2002) improves

245 sensitivity in high biomass regions and is used to derive the MODIS phenology product (Zhang

246 et al., 2003). As such, the NBAR-derived EVI time series data are used to detect vegetation

247 phenology metrics in this study.

248

249 **2.3 The synthetic time series of shortwave broadband albedo and vegetation index**

250

251 The STARFM algorithm is used to derive the synthetic time series of daily albedo and enhanced

252 vegetation index at a 30m spatial resolution. STARFM blends the Landsat and MODIS data by

253 using the spatially and temporally weighted difference between paired MODIS and Landsat

254 pixels from same day images to predict intermediate values on MODIS dates and create a

255 comprehensive phenological record (Gao et al., 2006). In this study both the synthetic daily

256 shortwave broadband albedo and the EVI values were generated utilizing STARFM from the

257 paired images of Landsat and MODIS albedo and the paired images of NBAR-derived EVI to

258 model the non-linear change over the entire period (Emelyanova et al., 2013). STARFM is

259 applied directly to the shortwave broadband albedo and EVI values rather than the underlying

260 surface reflectance in order to reduce the mismatch in bandwidths between the Landsat and

261 MODIS data. The daily MODIS NBAR-derived EVI (Collection V006) and Landsat EVI are

262 fused to build EVI time-series for deriving the vegetation phenology. Daily 30 m spatial

10

263    resolution STARFM images were generated for the entire year of 2007at Harvard Forest, Santa

264    Rita in 2011 and Walker Branch in 2005. The spatial extent of STARFM images is 16 km by 14

265    km at Harvard Forest and 5 km by 5 km at both the Santa Rita and Walker Branch sites. To

266    facilitate a more robust analysis of the surface heterogeneity, a larger plot was selected for

267    statistics at the Harvard Forest site (16 km by 14 km). This was done to include most of land

268    classes of typical forested areas of the northeastern United States (evergreen forest, deciduous

269    forest, grassland, inland water bodies and residential areas). The cloud, cloud shadow and snow

270    flags created by the LEDAPS algorithm were applied to select clear sky snow-free Landsat 5 TM

271    images prior to processing in STARFM (Table 2).

272

273    The phenology metrics (e.g. onset of vegetation green-up) were retrieved by applying the

274    piecewise logistic function to the synthetic time series snow-free daily EVI (Zhang et al., 2003).

275    No further smoothing processes was performed over the synthetic time series data before fitting

276    the piecewise logistic function.

277

278    Table 2. The acquisition dates of Landsat 5 TM images used for the Harvard Forest, Walker

279    Branch, and Santa Rita sites

| Site | Harvard Forest (year-month-day) | Walker Branch (year-month-day) | Santa Rita (year-month-day) |
|---|---|---|---|
| Landsat 5 TM Data | 2007-02-11 2007-03-30 2008-04-18* 2007-06-19 2007-09-07 | 2005-02-22 2005-03-10 2005-05-13 2005-09-18 2005-10-04 2005-10-20 | 2011-01-13 2011-01-29 2011-02-14 2011-03-02 2011-03-18 2011-04-03 2011-05-21 2011-06-22 2011-10-12 2011-10-28 |

280
281    * Landsat obtained from 2008-04-18 is utilized for the spring period as there was no available
282    cloud free imagery in 2007 and no disturbance/change between year 2007 and 2008.
283

284    **2.4 Surface heterogeneity analysis**

285

286    The heterogeneity of the Enhanced Vegetation Index (EVI) and shortwave broadband blue sky

287    albedo is analyzed by considering the standard deviation (Eq. 3) and difference between the

288    maximum and minimum values (Eq. 4) within the moderate grid (480 m) using the 30 m

289    STARFM synthetic datasets. Recognizing that the actual grid size of the so-called "500 m"

290    MODIS gridded product is 463 m, in this study the analysis is performed for each 480 m grid (16

291    by 16 Landsat pixels) within the subsets of the three sites.

292

293    $$Y_{480m-stdv} = \sqrt{\left(\sum_{i=1}^{N}\left(\bar{x}_{30m} - x_{i_{30m}}\right)^2\right)/(N-1)} \qquad (3)$$

294

295    $$Y_{480m-diff} = x_{max(30m)} - x_{min(30m)} \qquad (4)$$

296

297    $$\bar{Z}_{480m} = \left(\sum_{j=1}^{M} Y_{j_{480m}}\right)/M \qquad (5)$$

298

299    Where x refers to vegetation index or shortwave broadband blue sky albedo at 30 m spatial

300    resolution. *N* is the total number of 30 m clear sky pixels within each 480 m grid. *M* is the

301    number of 480 m grids within the study area. $Y_{480m-stdv}$ and $Y_{480m-diff}$ are the standard deviation

302    and difference of the maximum and minimum values within the 480m grid respectively. $\bar{Z}_{480m}$ is

303    the mean value of standard deviation ($Y_{480m-stdv}$) or difference of maximum and minimum ($Y_{480m-}$

304    $_{diff}$) values within the study area. These measures reflect the degrees of heterogeneity within a

305    MODIS pixel from Landsat pixel resolution

306

307    The heterogeneity and spatial representativeness of the NEON sites were also analyzed using a

308    semivariogram analysis (Carroll and Cressie, 1996; Matheron, 1963). The semivariogram is one

309    of  the most efficient tools to reveal the spatial variability of land surfaces and describe the

310    surface heterogeneity and spatial representativeness (Román et al., 2009; Woodcock et al.,

311    1988a, 1988b). Albedo spatial representativeness analysis was performed using semivariograms

312    created from the 30 m Landsat data to evaluate the surface heterogeneity of the regions around

313    the 20 NEON core ground towers (Román et al., 2009; Wang et al., 2014, 2012). The spatial

314    representativeness of the ground measurements for moderate spatial resolution satellite products

315    (e.g. MODIS, VIIRS) is evaluated at each NEON site. Although gridded as a 500 m product, the

316    MCD43A BRDF/albedo/NBAR products are generated from multi-angular surface reflectance

317    observations with varied footprints. As such, it is difficult to determine the exact footprint of one

318    MODIS gridded albedo pixel. Campagnolo et al. (2016) showed that the effective spatial

319    resolution of 500 m gridded MODIS BRDF/albedo/ NBAR product at mid latitudes is around

320    833 m by 618 m. Therefore, we analyzed the spatial representativeness of each site based on a

321    conservatively larger area. The ground measurements can be used to appropriately evaluate

322    moderate spatial resolution remote sensing products if the surface is spatially homogenous within

323    the larger area.  The variogram estimator is fitted to a spherical model to derive spatial attributes

324    (range, sill and nugget effect). The scale requirement index ($R_{se}$) (Eq. 6) (Román et al., 2009)

325    derived from the semivariogram analysis measures the relative spatial variation in albedo

326    considering both the footprint of the ground instrument and the surrounding landscape. The

327    surface is spatially representative with respect to the MODIS footprint when the $R_{se}$ is less than

328    0.243 (Román et al., 2009).

329    $R_{se} = \exp\left[-\sqrt{(g/a_x)^2 + (g/a_{1.5x})^2}\right]; x = 1.0 km$         (6)

330    Where:

331     $g = 2H\tan(FOV)$         (7)

332    $a$ is the range of two Landsat subsets of sizes $x$ and $1.5x$; $H$ is the height of the field albedometer;

333    $FOV$[degrees] is the half field-of-view of the albedometer; $g$ is the footprint of ground albedo

334    measurements. The site is spatially representative when $g>=a_x$ and $g>= a_{1.5x}$ so that the Rse

335    values are between [0.0, $e^{-\sqrt{2}} \approx 0.243$].

336

337    The sill is the ordinate value of the range at which the variogram levels off to an asymptote and

338    describes the maximum semivariance. Smaller sill values indicate less variation in albedo and a

339    more homogenous surface. Note that the spatially representative analysis is only applicable to

340    moderate resolution satellite measurements such as albedo and in no way reflects the suitability

341    of the site as a flux tower. Spatially representative analysis is not necessarily required to validate

342    fine spatial resolution satellite products (e.g. Landsat) as the footprints of the tower

343    measurements are larger than the Landsat pixel size.

344

345    **3.  Results and Discussion**

346    **3.1 Land surface heterogeneity**

347

348    The temporal standard deviation and difference of maximum and minimum shortwave

349    broadband blue sky albedo and EVI over a 16 km by 14 km area at the Harvard Forest site

13

350    computed using Eq. (1-4) is shown in Fig. 2. The spatial extent of this subset is the same as that

351    shown in Fig. 5 with the Ameriflux flux tower located at the center. The land cover of this area

352    includes evergreen forest, deciduous forest, grassland, several inland water bodies and residential

353    areas. As shown in Fig. 2, albedo is more heterogeneous during the snow-covered period with

354    the highest albedo values over completely snow-covered surfaces and relatively low albedo over

355    the forested areas where complete snow cover is rare. The maximum albedo within the study

356    area is 0.9 while the minimum albedo is less than 0.1. The mean of the difference between

357    maximum and minimum albedo over the entire study area is around 0.2 during the snow-covered

358    period and reduced to around 0.1 during the snow-free period. The standard deviation of the

359    albedo measurements shows similar trends to the mean of the difference between maximum and

360    minimum albedo. The mean albedo standard deviation is at around 0.014 during the snow-free

361    period and increases to 0.05 during the snow-covered period. EVI is relatively homogeneous

362    during the dormant period and more heterogeneous during the growing season due to the

363    different land cover growth patterns. The mean of the difference between maximum and

364    minimum EVI over the study area is around 0.35 during the growing season; which is about 0.1

365    higher than the dormant period. The mean EVI standard deviation during the growing season is

366    about 0.02 higher than the values during the dormant period.

367



368

369

370
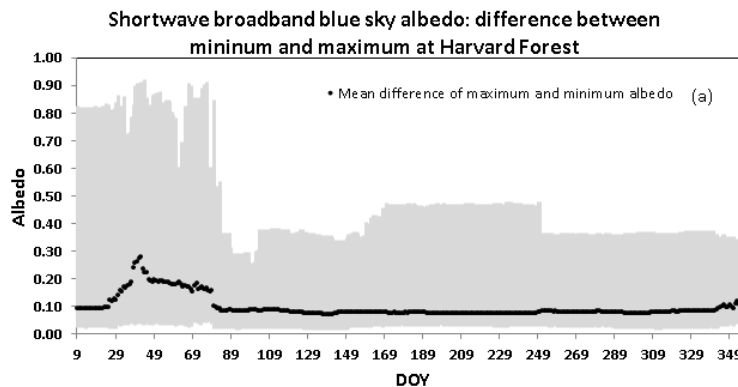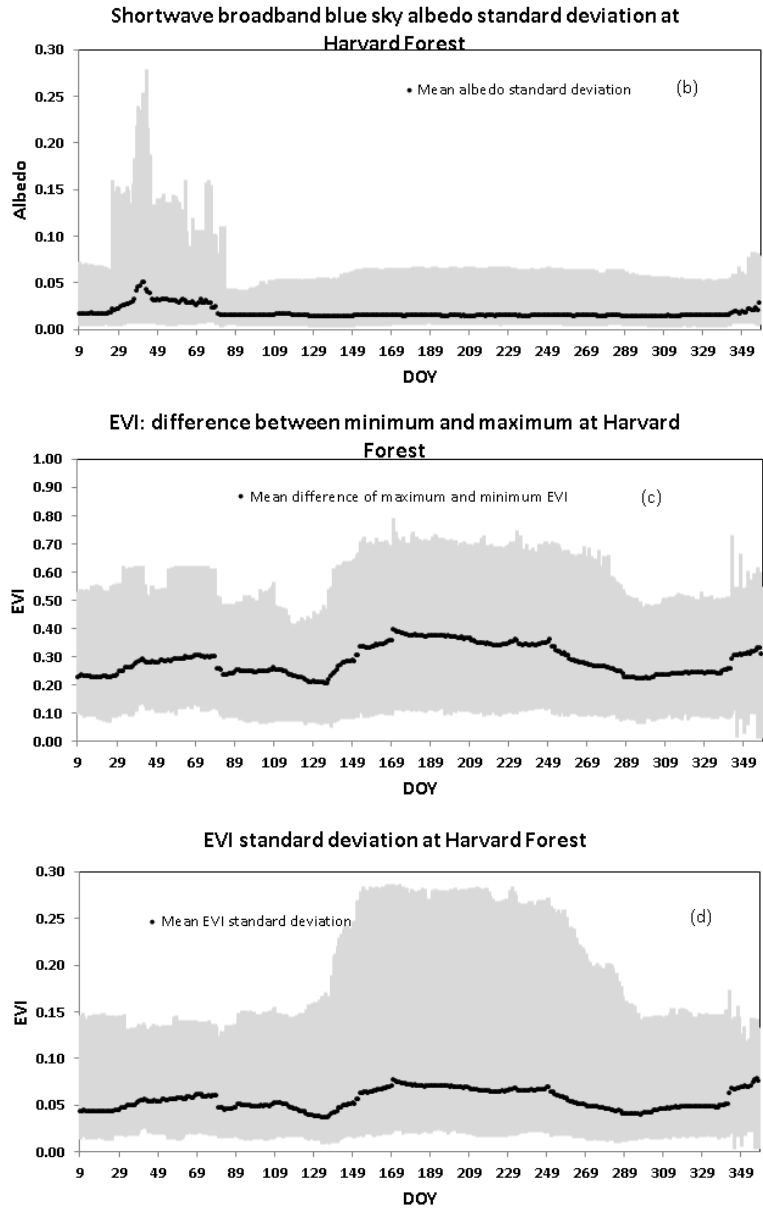
371
372 Fig. 2. Temporal plot showing the difference of the maximum and minimum (a) and the standard

373 deviation (b) of shortwave broadband blue sky albedo within the 480 m spatial resolution grids

374 based on 30 m synthetic albedo times series at the Harvard Forest in 2007; Temporal plot of the

375 difference of the maximum and minimum (c) and the standard deviation (d) of EVI within 480 m

376 spatial resolution pixels based on 30 m synthetic EVI time series at the Harvard Forest in 2007.

377 The subset area is 16 km by 14 km. The gray area represents the range of maximum and

378 minimum values within the study area.

379

380   The big ranges in the standard deviation and maximum and minimum difference of both albedo
381   and EVI indicate that there is significant spatial variation in the land surface of the Harvard
382   Forest at MODIS pixel scales. Therefore, fine spatial resolution data is required to accurately
383   quantify the effects of vegetation changes on the terrestrial carbon cycle and climate change at
384   the patch-scale (Goward et al., 2008; Masek et al., 2013; Shuai et al., 2011).
385
386   Here we investigate the representativeness of the albedos that will be measured from NEON
387   towers for the validation of the MODIS albedo product based on the surface heterogeneity and
388   spatial representativeness analysis (Fig. 3). While this analysis focuses on the MODIS albedo
389   product, the results are applicable to other satellite products with similar spatial resolutions (e.g.
390   VIIRS). Most of the NEON core terrestrial sites with tower height higher than 10m are relatively
391   homogenous and the ground measured albedo is spatially representative of the MODIS albedo
392   during both the leaf-on and leaf-off seasons (Table 3). Although the $R_{se}$ values of all the 8 m
393   tower sites are larger than 0.243, the sill values of Konza Prairie Biological Station, Central
394   Plains Experimental Range, Santa Rita Experimental Range, Toolik Lake and 20m tower height
395   Guanica Forest, Yellowstone Northern Range and Upper Waiakea Forest Reserve sites are low at
396   less than 0.0005. These sites can also be considered homogenous and representative. Fig. 4
397   shows that the difference between MODIS and ground measured albedo at the Santa Rita site is
398   less than 0.02. The Caribou Creek taiga, Woodworth, LBJ National Grassland, and Niwot Ridge
399   Mountain Research Station sites represent grassland and forest ecotones and are particularly
400   heterogeneous and may not serve as ideal validation sites for moderate resolution satellite
401   products. In general, shrub and open woodland sites, located in areas with little human activity
402   and no water bodies nearby, are all spatially representative. It should be noted that just as the
403   location of the NEON core towers has been optimized for flux measurements, the actual height
404   of the towers and the placement of the downward radiometers has also been optimized for flux
405   measurements and is governed by the height of the surrounding canopy. Although sites located
406   in heterogenous regions (e.g. the Caribou Creek taiga) are not spatially representative for
407   moderate spatial resolution albedo validation, the footprints of these tower albedo are typically
408   larger than a single pixel of high spatial resolution albedo (e.g. Landsat, Sentinel 2). As such,
409   these sites can still be used to evaluate the accuracy of higher spatial resolution albedo products.
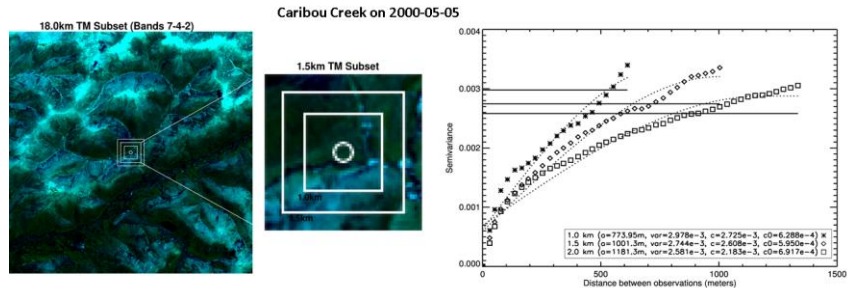
410



411
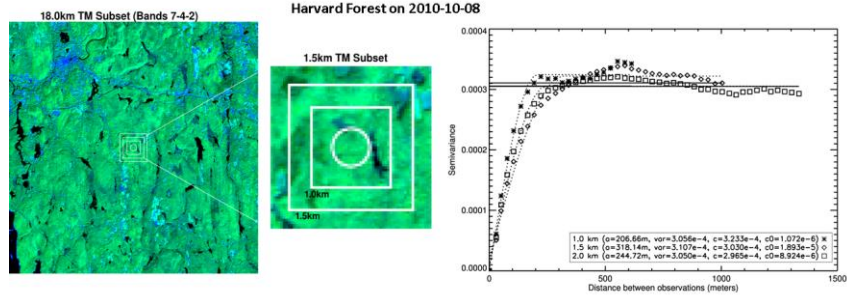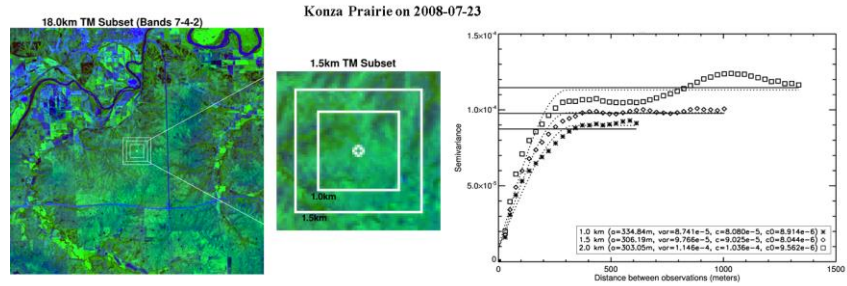
412
413
414
415 Fig. 3 Shortwave reflectance composite (TM Bands 7–4–2) and corresponding semivariogram
416 functions, variogram estimator (points), spherical model (dotted curves), and sample variance
417 (solid straight lines) using regions of 1.0 km (asterisks), 1.5 km (diamonds), and 2.0 km
418 (squares), centered over Harvard Forest on 2010-10-08, Konza Prairie on 2008-07-23, Caribou
419 Creek - Poker Flats Watershed on 2000-05-05. The circles show the footprint of tower albedo
420 measurements calculated from the tower height and albedometer FOV.

17

Harvard Forest Albedo

Santa Rita Albedo

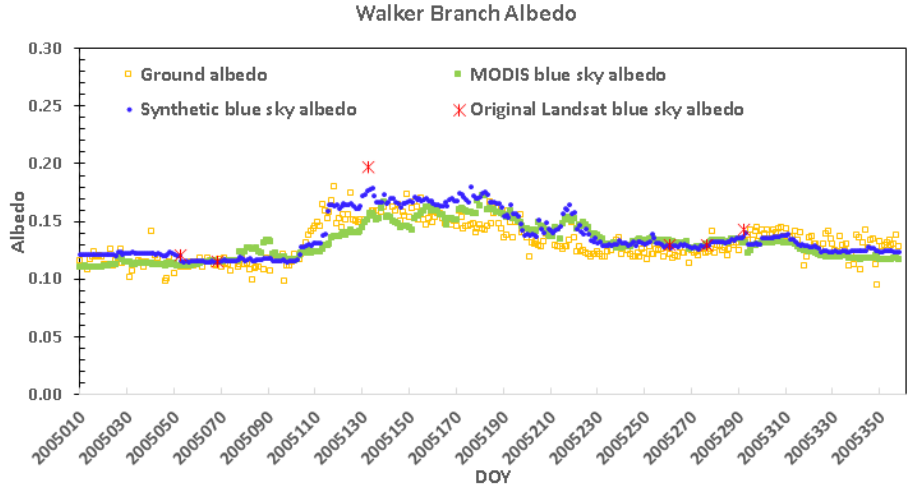Walker Branch Albedo

421

422
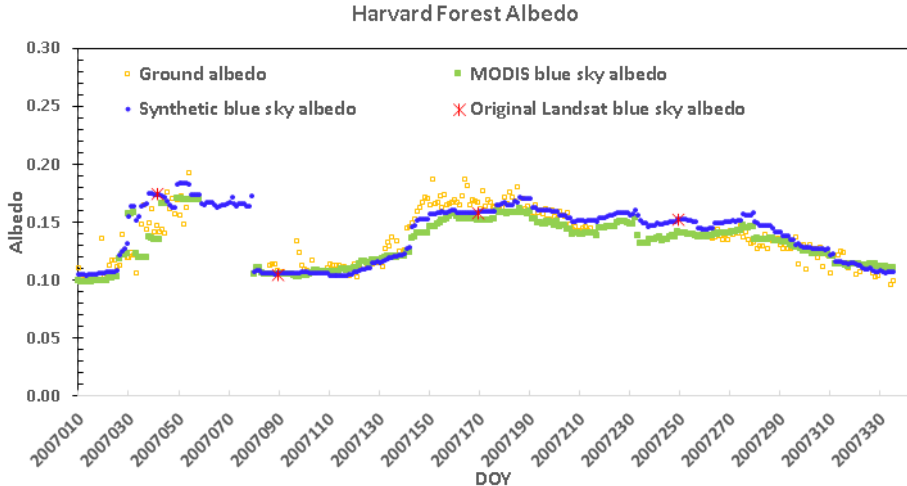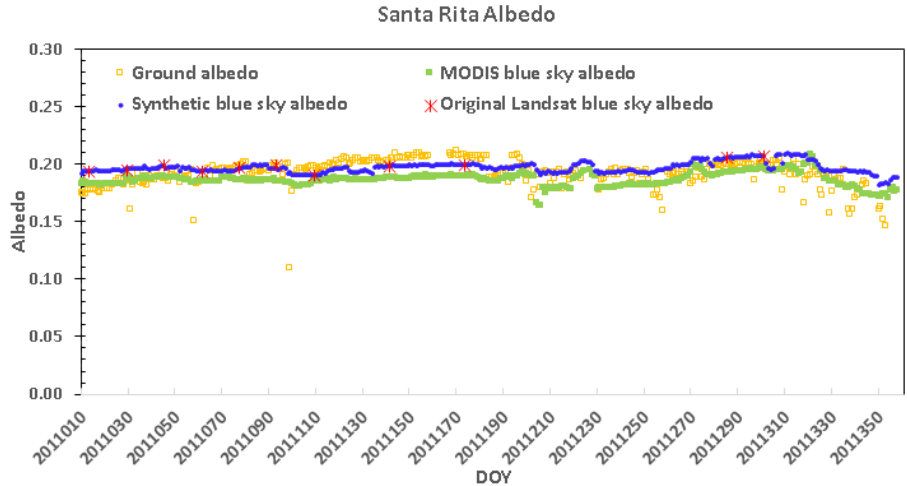
423
424
425        Fig. 4. Comparison of synthetic time series of blue-sky albedo with ground-measured

426        albedo, MODIS blue-sky albedo, and Landsat blue-sky albedo over Harvard Forest

427        (2007), Santa Rita (2011), and Walker Branch (2005) sites.  Synthetic, ground-measured,

428    and MODIS albedo measurements were obtained on a daily basis.  Landsat 5

429    measurements were derived from all cloud-free images available in each year (Table 2)

430 Table 3. Spatial representativeness status of NEON sites for moderate spatial resolution satellite
431 albedo product validation. The highest "sill" values of the three analyzed spatial regions sites
432 (1.0 km, 1.5 km and 2.0 km) in the semivariogram analysis are presented here.

| Domain Number | Site Name | $R_{se}$ | | Sill | |
|---|---|---|---|---|---|
| | | Leaf on | Leaf off | Leaf on | Leaf off |
| D01 | Harvard Forest | 0.0726 | 0.2104 | 0.0003 | 0.0003 |
| D02 | Smithsonian Conservation Biology Institute | 0.0148 | 0.0253 | 0.0001 | 0.0002 |
| D03 | Ordway-Swisher Biological Station | 0.0618 | N/A[§] | 0.0003 | N/A |
| D04 | Guanica Forest | 0.2705 | N/A | 0.0001 | N/A |
| D05 | University of Notre Dame Environmental Research Center | 0.1408 | 0.0673 | 0.0011 | 0.0004 |
| D06 | Konza Prairie Biological Station | 0.6395 | 0.6531 | 0.0001 | 0.0005 |
| D07 | Oak Ridge | 0.0469 | 0.1777 | 0.0003 | 0.0006 |
| D08 | Talladega National Forest | 0.0341 | N/A | 0.0001 | N/A |
| D09 | Woodworth | 0.5626 | 0.5738 | 0.0014 | 0.0011 |
| D10 | Central Plains Experimental Range | N/A | N/A | 0.0002 | 0.0002 |
| D11 | LBJ National Grassland | N/A | N/A | 0.0005 | 0.0015 |
| D12 | Yellowstone Northern Range (Frog Rock) | 0.5222 | 0.5209 | 0.0004 | 0.0004 |
| D13 | Niwot Ridge Mountain Research Station | 0.5970 | 0.7196 | 0.0004 | 0.0011 |
| D14 | Santa Rita Experimental Range | N/A | N/A | 0.0002 | 0.0002 |
| D15 | Onaqui-Ault | 0.5873 | 0.5365 | 0.0001 | 0.0002 |

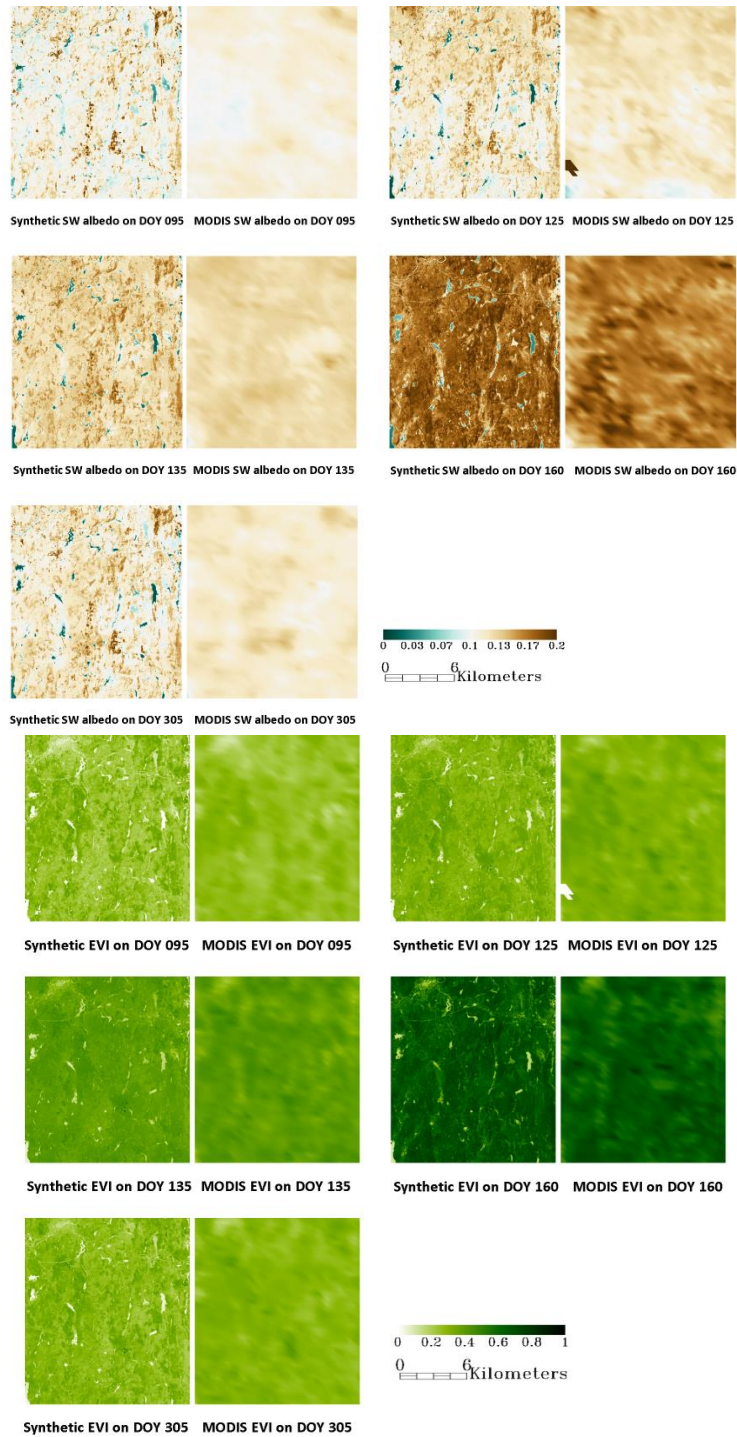| | | | | | |
|---|---|---|---|---|---|
| D16 | Wind River Experimental Forest | 0.0085 | N/A | 0.0007 | N/A |
| D17 | San Joaquin Experimental Range | 0.0393 | 0.0636 | 0.0001 | 0.0003 |
| D18 | Toolik Lake | N/A | N/A | 0.0002 | |
| D19 | Caribou Creek - Poker Flats Watershed | N/A | N/A | 0.0008 | 0.0034 |
| D20 | Upper Waiakea Forest Reserve | 0.4609 | N/A | 0.0001 | N/A |

433 [§]N/A represents data not available (evergreen vegetation sites for leaf off (site 3, 4, 16, 19, and
434 20), no clear sky images available (site 8), or sites where the semivariogram curve fails to fit the
435 spherical model (site 10, 11, 14, 18, and 19)).

436 **3.2 Synthetic shortwave albedo and EVI for land surface dynamics monitoring**

437 The synthetic times series of 30 m broadband shortwave blue sky albedo is averaged according

438 to the footprint of the tower albedometer for comparison with ground measurements. The

439 albedos at Harvard Forest are around 0.19 during winter as snow beneath the forest canopy

440 increases reflectance. The albedo decreases with the snowmelt and then increases to a maximum

441 of about 0.16 during the course of the growing season (Fig. 4). Gaps in the data record are a

442 result of missing ground albedo measurements from DOY 55 to 84 at the Harvard forest tower.

443 The MODIS and synthetic albedo were not retrieved from around the Harvard Forest tower from

444 DOY 59 to 79 due to the lack of valid MODIS reflectance data. Unsurprisingly, the synthetic 30

445 m albedo time series captures finer spatial characteristics than the MODIS data alone while

446 maintaining similar seasonal dynamics (Fig. 5). The Santa Rita site is relatively stable with

447 albedos remaining near 0.2 all year (appropriate for such a semiarid open shrub land site). The

448 seasonal dynamics at this site are mainly dominated by the change of soil moisture (Sanchez-

449 Mejia et al., 2014). Walker Branch is a deciduous forest site with no winter snow cover. As such,

450 the albedo is lower than Harvard Forest in the winter (~0.12) and increases to a maximum of

451 0.17 during the growing season. The RMSEs of the synthetic blue sky albedo as compared to the

452 tower albedo values are 0.013, 0.009 and 0.012 for the Harvard Forest, Santa Rita and Walker

453 Branch sites respectively and the biases for the three sites are 0.002, 0.003 and 0.006

454 respectively. The footprint of the tower albedo measurements is close (Santa Rita) to or larger

455 than (Harvard Forest and Walker Branch) the 30 m Landsat and synthetic albedo pixel sizes, yet

456    smaller than the effective spatial resolution of MODIS albedo. Landsat and synthetic albedo

457    values were averaged according to the tower footprints for comparison, as such the area

458    mismatch between combined Landsat and synthetic pixels and the ground footprint is less than

459    the mismatch between ground footprint and a MODIS pixel. As a result, the Landsat and

460    synthetic albedo values are slightly closer to the tower albedos than the MODIS albedo values

461    (Fig. 4) over the three sites. The RMSE of the more homogenous shrub land (Santa Rita) is lower

462    than the values at forest sites (Harvard Forest and Walker Branch). The combined accuracy of

463    the synthetic blue sky albedo at these all three sites (RMSE 0.016, bias −0.013) is close to the

464    values in Shuai et al. (2011) and meets the absolute accuracy requirement of 0.02–0.05 (Sellers

465    et al., 1995) required by modelers. The accuracy of the synthetic time series of blue sky albedo

466    values is affected by the number and quality of the finer spatial resolution data. For example,

467    only one Landsat image is available during the growing season (2005-05-13) at Walker Branch

468    and this Landsat albedo value is 0.04 higher than the measured ground albedo. This observation

469    is close to the edge of a cloud and is potentially contaminated by a thin cloud not detected with

470    the Landsat cloud mask. Enhanced temporal resolution coverage of finer scale satellite data over

471    these sites would obviously improve the synthetic time series results. The availability and

472    improved technical capabilities (1.38μm cirrus band and the improved radiometric resolution) of

473    Landsat 8 (2013) and Sentinel-2A (2015) obviously will contribute significantly to improved fine

474    scale synthetic time series results. The synthetic 30 m albedo show a wider data range than the

475    stand-alone MODIS albedo. This is because spatial details captured at the Landsat 30 m

476    resolution are mixed/smoothed at the MODIS 500 m resolution. However, the number of original

477    clear sky Landsat 5 observations is very limited at the Harvard Forest and Walker Branch sites

478    with only four at Harvard Forest in 2007 and six at Walker Branch in 2005. The Santa Rita site,

479    in a semiarid area, had 11 original clear sky Landsat 5 observations in 2011 (Table 2). However,

480    in all cases, the daily synthetic EVI and albedo time series significantly expand the spatial and

481    temporal resolution of datasets for climate study.

482

Synthetic SW albedo on DOY 095   MODIS SW albedo on DOY 095

Synthetic SW albedo on DOY 125   MODIS SW albedo on DOY 125

Synthetic SW albedo on DOY 135   MODIS SW albedo on DOY 135

Synthetic SW albedo on DOY 160   MODIS SW albedo on DOY 160

Synthetic SW albedo on DOY 305   MODIS SW albedo on DOY 305

0   0.03  0.07   0.1  0.13  0.17   0.2

0           6  Kilometers

Synthetic EVI on DOY 095   MODIS EVI on DOY 095

Synthetic EVI on DOY 125   MODIS EVI on DOY 125

Synthetic EVI on DOY 135   MODIS EVI on DOY 135

Synthetic EVI on DOY 160   MODIS EVI on DOY 160

Synthetic EVI on DOY 305   MODIS EVI on DOY 305

0   0.2   0.4   0.6   0.8   1

0           6  Kilometers

Fig. 5. The synthetic time series and MODIS shortwave broadband blue sky albedo and EVI at Harvard Forest subset (16 km by 14 km) on DOY 95, 125, 135, 160 and 305 in 2007.

22

491   The phenological metrics derived from multi-day composite datasets can mask high-frequency
492   vegetation changes (Ju et al., 2010; McKellip et al., 2005; Narasimhan and Stow, 2010). Shuai et
493   al. (2013) showed that subtle details in growth stages can be captured from daily MODIS
494   NBAR-derived EVI. Currently the temporal resolution of the Landsat data makes it difficult to
495   capture vegetation phenological metrics, particularly in the shoulder seasons (e.g. green-up,
496   senescence) which are important in analyzing the impacts of climate change. The MODIS-
497   Landsat derived synthetic daily 30 m spatial resolution times series of EVI can be used to
498   monitor complex land surface characteristics, especially rapidly changing seasonal dynamics.
499   The phenology patterns of the vegetation were well captured by the synthetic EVI time series at
500   Harvard Forest in 2007 (Fig. 5; Fig. 6). The logistic model fitted EVI dates agrees well with the
501   synthetic temporal EVI dates. The ground phenology information at Harvard Forest was
502   measured every 4 days during the green-up period. In 2007, the green-up date determined from
503   the synthetic 30 m data sets (Day Of Year (DOY) 120) matches well with the field measured
504   date (124). The green-up date derived from 500 m MODIS product (MCD12Q2) (Zhang et al.,
505   2003) was considerably earlier at DOY 115. The difference in the onset of green-up within a
506   single MODIS pixel can be more than 10 days over the same forest type (Fig. 6b). This spatial
507   variation in phenology could be caused by species distribution or small scale microclimates.
508   Small scale microclimates have previously been shown to result in large phenological variability
509   within hundreds of meters (Klosterman et al., 2014; Vitasse et al., 2009). The temporal variation
510   of synthetic EVI times series however, captures the development of foliage stages at the Santa
511   Rita site (Fig. 6c). The shrubs started to green-up on DOY 220 and reached the first peak on
512   DOY 230 and the second peak on DOY 260 in 2011. The single year analysis in this study
513   demonstrate an ability to derive temporal vegetation variations at high spatial resolution using a
514   variety of data fusion techniques. Further work is required for different vegetation types over a
515   longer period to extend this study to completely assess the implication of land surface
516   heterogeneity on the phenological analyses.
517
518   The synthetic EVI also shows greater spatial detail than the MODIS EVI, especially over more
519   heterogeneous surfaces. This improves our ability to characterize spatial variations in EVI across
520   species and communities. The maximum EVI standard deviation within a 480 m grid at Harvard
521   Forest is over 0.25 and the difference of maximum and minimum EVI within the 480 m grid can

522  be as high as 0.7 during the growing season (Fig. 2). In addition, the boundaries between forest

523  types and water bodies are very clear in the synthetic EVI but difficult to identify in the MODIS

524  EVI.

525
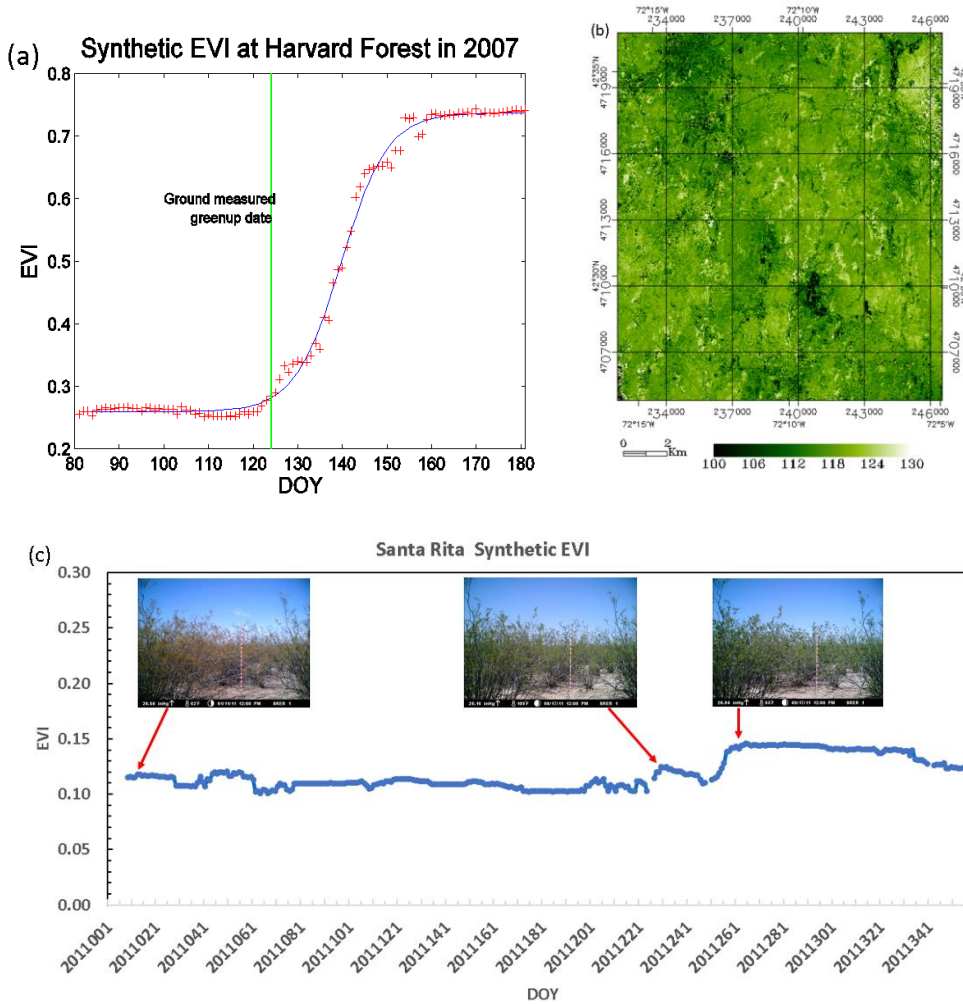


526
527



528
529
530  Fig. 6. (a) Temporal plot of synthetic time series EVI (red +) and logistic model fit (blue line) at
531  Harvard Forest flux tower in 2007, (b) the onset (DOY) of green-up at Harvard Forest subset (16
532  km by 14 km) and (c) the temporal plot of synthetic EVI and phenocam photos at Santa Rita site.

533

534  **4. Conclusion**

535

536  The MODIS-Landsat coupled synthetic albedo and EVI times series are able to capture the land

537  surface dynamics at high spatial resolution.  Such a capability lays the ground work for long-

538  term monitoring of vegetation phenology at the stand scale in response to climate change,

539   disturbance regimes, and other drivers. The heterogeneity analyses of all of the NEON sites and

540   of the three Ameriflux sites used in this study indicates that the range of EVI and albedo within

541   moderate spatial resolution grids is very large and higher spatial resolution vegetation index and

542   albedo values are necessary to understand how individual vegetation types are responding to

543   environmental forcing. The daily high spatial resolution synthetic vegetation index time series

544   enhances the monitoring of vegetation phenology change. At the Harvard Forest site, the

545   difference between the synthetic EVI determinations and the ground measured green-up date is

546   within 4 days. This suggests that over mixed deciduous broadleaf and evergreen needleleaf forest

547   ecosystems, the modeled phenology can be used to capture vegetation temporal variations at the

548   landscape scale. The synthetic albedo time series match well with the ground albedo values with

549   RMSE and bias less than 0.013 and within $\pm 0.006$ respectively over the three Ameriflux sites.

550   As more of the spatially representative NEON core site towers are established, continued

551   comparisons and validation can be done to monitor seasonal and temporal trends. The

552   establishment of the NEON core sites will contribute significantly to our knowledge of a

553   diversity of ecosystems and provide key validation measurements for both satellite data and

554   future models and simulations. However, as noted, the NEON sites were originally selected for

555   applicability to serve as flux sites and not necessarily the best placements to evaluate satellite

556   products, and therefore, this analysis of spatial representativeness is important in defining the

557   appropriate usage of these NEON data. The observations of higher resolution surface phenology

558   and energy change from the synthetic time series data will be continued with the newer

559   generation of satellites including Landsat 8 Operational Land Imager (OLI), Sentinel-2A/B

560   MultiSpectral Instrument (MSI), and Suomi-NPP Visible Infrared Imager Radiometer Suite

561   (VIIRS) satellite sensors.

562

563   **Acknowledgement**

564

25

577

578  **Reference:**
579

580  Baldocchi, D., Falge, E., Wilson, K., 2001. A spectral analysis of biosphere – atmosphere trace
581      gas flux densities and meteorological variables across hour to multi-year time scales. Agric.
582      For. Meteorol. 107, 1–27. doi:10.1016/S0168-1923(00)00228-8

583  Campagnolo, M.L., Sun, Q., Liu, Y., Schaaf, C., Wang, Z., Román, M.O., 2016. Estimating the
584      effective spatial resolution of the operational BRDF, albedo, and nadir reflectance products
585      from MODIS and VIIRS. Remote Sens. Environ. 175, 52–64. doi:10.1016/j.rse.2015.12.033

586  Carroll, S.S., Cressie, N., 1996. A comparison of geostatistical methodologies used to estimate
587      snow water equivalent. Water Resour. Bull. 32, 267–278. doi:10.1111/j.1752-
588      1688.1996.tb03450.x

589  Churkina, G., Schimel, D., Braswell, B.H., Xiao, X.M., 2005. Spatial analysis of growing season
590      length control over net ecosystem exchange. Glob. Chang. Biol.

591  Cleland, E.E., Chiariello, N.R., Loarie, S.R., Mooney, H.A., Field, C.B., 2006. Diverse responses
592      of phenology to global changes in a grassland ecosystem. Proc. Natl. Acad. Sci. U. S. A.
593      103, 13740–13744.

594  Dirmeyer, P.A., Shukla, J., 1994. Albedo as a modulator of climate response to tropical
595      deforestation. J. Geophys. Res. 99, 20863–20877.

596  Emelyanova, I. V., McVicar, T.R., Van Niel, T.G., Li, L.T., van Dijk, A.I.J.M., 2013. Assessing
597      the accuracy of blending Landsat–MODIS surface reflectances in two landscapes with
598      contrasting spatial and temporal dynamics: A framework for algorithm selection. Remote
599      Sens. Environ. 133, 193–209. doi:10.1016/j.rse.2013.02.007

600  Friedl, M. a, Gray, J.M., Melaas, E.K., Richardson, A.D., Hufkens, K., Keenan, T.F., Bailey, A.,
601      O'Keefe, J., 2014. A tale of two springs: using recent climate anomalies to characterize the
602      sensitivity of temperate forest phenology to climate change. Environ. Res. Lett. 9, 054006.
603      doi:10.1088/1748-9326/9/5/054006

604  Ganguly, S., Friedl, M. a., Tan, B., Zhang, X., Verma, M., 2010. Land surface phenology from
605      MODIS: Characterization of the Collection 5 global land cover dynamics product. Remote
606      Sens. Environ. 114, 1805–1816. doi:10.1016/j.rse.2010.04.005

607  Gao, F., Masek, J., Schwaller, M., Hall, F., 2006. On the blending of the Landsat and MODIS
608      surface reflectance: predicting daily Landsat surface reflectance. IEEE Trans. Geosci.
609      Remote Sens. 44, 2207–2218. doi:10.1109/TGRS.2006.872081

26

610  Goward, S.N., Masek, J.G., Cohen, W., Moisen, G., Collatz, G.J., Healey, S., Houghton, R. a.,
611      Huang, C., Kennedy, R., Law, B., Powell, S., Turner, D., Wulder, M. a., 2008. Forest
612      Disturbance and North American Carbon Flux. Eos, Trans. Am. Geophys. Union 89, 105.
613      doi:10.1029/2008EO110001

614  Hall, A., 2004. The Role of Surface Albedo Feedback in Climate. J. Clim. 17, 1550–1568.
615      doi:10.1175/1520-0442(2004)017<1550:TROSAF>2.0.CO;2

616  Hamilton, M.P., Graham, E. a., Rundel, P.W., Allen, M.F., Kaiser, W., Hansen, M.H., Estrin,
617      D.L., 2007. New Approaches in Embedded Networked Sensing for Terrestrial Ecological
618      Observatories. Environ. Eng. Sci. 24, 192–204. doi:10.1089/ees.2006.0045

619  Hansen, J., Ruedy, R., Sato, M., Lo, K., 2010. Global Surface Temperature Change. Rev.
620      Geophys. 48, 1–29. doi:10.1029/2010RG000345.1.INTRODUCTION

621  Hansen, J., Sato, M., Ruedy, R., Lo, K., Lea, D.W., Medina-elizade, M., 2006. Global
622      temperature change. Proc. Natl. Acad. Sci. U. S. A. 103, 14288–14293.

623  He, T., Liang, S., Wang, D., Shuai, Y., Yu, Y., 2014. Fusion of satellite land surface albedo
624      products across scales using a multiresolution tree method in the north central United States.
625      IEEE Trans. Geosci. Remote Sens. 52, 3428–3439. doi:10.1109/TGRS.2013.2272935

626  Hilker, T., Wulder, M. a., Coops, N.C., Seitz, N., White, J.C., Gao, F., Masek, J.G., Stenhouse,
627      G., 2009. Generation of dense time series synthetic Landsat data through data blending with
628      MODIS using a spatial and temporal adaptive reflectance fusion model. Remote Sens.
629      Environ. 113, 1988–1999. doi:10.1016/j.rse.2009.05.011

630  Huete, A., Didan, K., Miura, T., Rodriguez, E.P., Gao, X., Ferreira, L.G., 2002. Overview of the
631      radiometric and biophysical performance of the MODIS vegetation indices. Remote Sens.
632      Environ. 83, 195–213. doi:10.1016/S0034-4257(02)00096-2

633  Jin, Y., Schaaf, C.B., Gao, F., Li, X., Strahler, A.H., 2003. Consistency of MODIS surface
634      bidirectional reflectance distribution function and albedo retrievals: 1. Algorithm
635      performance. J. Geophys. Res. 108.

636  Jin, Y.B.S., Gao, F., Li, X., Strahler, A.H., Zeng, X., Dickinson, R.E., 2002. How does snow
637      impact the albedo of vegetated land surfaces as analyzed with MODIS data? Geophys. Res.
638      Lett. 29, 12–15. doi:10.1029/2001GL014132

639  Ju, J., Roy, D.P., Shuai, Y., Schaaf, C., 2010. Development of an approach for generation of
640      temporally complete daily nadir MODIS reflectance time series. Remote Sens. Environ.
641      114, 1–20. doi:10.1016/j.rse.2009.05.022

642  Kampe, T.U., 2010. NEON: the first continental-scale ecological observatory with airborne
643      remote sensing of vegetation canopy biochemistry and structure. J. Appl. Remote Sens. 4,
644      043510. doi:10.1117/1.3361375

645  Keller, M., Schimel, D.S., Hargrove, W.W., Hoffman, F.M., 2008. A continental strategy for the
646      National Ecological Observatory Network. Front. Ecol. Environ. 6, 282–284.
647      doi:10.1890/1540-9295(2008)6[282:ACSFTN]2.0.CO;2

648  Klosterman, S.T., Hufkens, K., Gray, J.M., Melaas, E., Sonnentag, O., Lavine, I., Mitchell, L.,
649      Norman, R., Friedl, M.A., Richardson, A.D., 2014. Evaluating remote sensing of deciduous
650      forest phenology at multiple spatial scales using PhenoCam imagery. Biogeosciences 11,
651      4305–4320. doi:10.5194/bg-11-4305-2014

652  Körner, C., Basler, D., 2010. Phenology Under Global Warming. Science (80-. ). 327, 1461–
653      1462. doi:10.1126/science.1186473

654  Law, B., Falge, E., Gu, L., Baldocchi, D., Bakwin, P., Berbigier, P., Davis, K., Dolman, A., Falk,
655      M., Fuentes, J., 2002. Environmental controls over carbon dioxide and water vapor
656      exchange of terrestrial vegetation. Agric. For. Meteorol. 113, 97–120. doi:10.1016/S0168-
657      1923(02)00104-1

658  Lewis, P., Barnsley, M., 1994. Influence of the sky radiance distribution on various formulations
659      of the earth surface albedo. Proc. Conf. Phys. Meas. Signatures Remote Sens.

660  Liang, L., Schwartz, M.D., Wang, Z., Gao, F., Schaaf, C.B., Tan, B., Morisette, J.T., Zhang, X.,
661      2014. A Cross Comparison of Spatiotemporally Enhanced Springtime Phenological
662      Measurements From Satellites and Ground in a Northern U.S. Mixed Forest. IEEE Trans.
663      Geosci. Remote Sens. 52, 7513–7526. doi:10.1109/TGRS.2014.2313558

664  Liang, S., Fang, H., Chen, M., Shuey, C.J., Walthall, C., Daughtry, C., Morisette, J., Schaaf, C.,
665      Strahler, A., 2002. Validating MODIS land surface reflectance and albedo products:
666      methods and preliminary results. Remote Sens. Environ. 83, 149–162. doi:10.1016/S0034-
667      4257(02)00092-5

668  Liu, J., Schaaf, C., Strahler, A., Jiao, Z., Shuai, Y., Zhang, Q., Roman, M., Augustine, J. a.,
669      Dutton, E.G., 2009. Validation of Moderate Resolution Imaging Spectroradiometer
670      (MODIS) albedo retrieval algorithm: Dependence of albedo on solar zenith angle. J.
671      Geophys. Res. 114, D01106. doi:10.1029/2008JD009969

672  Lofgren, B., 1995. Surface albedo-climate feedback simulated using two-way coupling. J. Clim.
673      8, 2543–2562.

674  Lucht, W., Schaaf, C.B., Strahler, a. H., 2000. An algorithm for the retrieval of albedo from
675      space using semiempirical BRDF models. IEEE Trans. Geosci. Remote Sens. 38, 977–998.
676      doi:10.1109/36.841980

677  Masek, J.G., Goward, S.N., Kennedy, R.E., Cohen, W.B., Moisen, G.G., Schleeweis, K., Huang,
678      C., 2013. United States Forest Disturbance Trends Observed Using Landsat Time Series.
679      Ecosystems 16, 1087–1104. doi:10.1007/s10021-013-9669-9

680  Masek, J.G., Vermote, E.F., Saleous, N.E., Wolfe, R., Hall, F.G., Huemmrich, K.F., Gao, F.,
681      Kutler, J., Lim, T., 2006. A Landsat Surface Reflectance Dataset. IEEE Geosci. Remote
682      Sens. Lett. 3, 68–72.

683  Matheron, G., 1963. Principles of geostatistics. Econ. Geol. 58, 1246–1266.
684      doi:10.2113/gsecongeo.58.8.1246

685  McKellip, R., Ryan, R.E., Blonski, S., Prados, D., 2005. Crop surveillance demonstration using a
686      near-daily MODIS derived vegetation index time series, in: Proceedings of the Third
687      International Workshop on the Analysis of Multi-Temporal Remote Sensing Images 2005.
688      pp. 54–58. doi:10.1109/AMTRSI.2005.1469839

689  Menzel, A., Fabian, P., 1999. Growing season extended in Europe. Nature 397, 659.
690      doi:10.1038/311558a0

691  Menzel, A., Sparks, T.H., Estrella, N., Koch, E., Aasa, A., Ahas, R., Alm-Kubler, K., Bissolli, P.,
692      Braslavska, O., Briede, A., Chmielewski, F.M., Crepinsek, Z., Curnel, Y., Dahl, A., Defila,
693      C., Donnelly, A., Filella, Y., Jatczak, K., Mage, F., Mestre, A., Nordli, O., Penuelas, J.,

694       Pirinen, P., Remisova, V., Scheifinger, H., Striz, M., Susnik, A., Viet, V., Arnold, J.H.,
695           Wielgolaski, F.-E., Zach, S., Zust, A., 2006. European phenological response to climate
696           change matches the warming pattern. Glob. Chang. Biol. 12, 1969–1976.

697   Myneni, R.B., Keeling, C.D., Tucker, C.J., Asrar, G., Nemani, R.R., 1997. Increased plant
698           growth in the northern high latitudes from 1981 to 1991. Nature 386, 698–702.

699   Narasimhan, R., Stow, D., 2010. Daily MODIS products for analyzing early season vegetation
700           dynamics across the North Slope of Alaska. Remote Sens. Environ. 114, 1251–1262.
701           doi:10.1016/j.rse.2010.01.017

702   Ollinger, S. V, Richardson, A.D., Martin, M.E., Hollinger, D.Y., Frolking, S.E., Reich, P.B.,
703           Plourde, L.C., Katul, G.G., Munger, J.W., Oren, R., Smith, M.L., Paw U, K.T., Bolstad, P.
704           V, Cook, B.D., Day, M.C., Martin, T.A., Monson, R.K., Schmid, H.P., 2008. Canopy
705           nitrogen, carbon assimilation, and albedo in temperate and boreal forests: Functional
706           relations and potential climate feedbacks. Proc. Natl. Acad. Sci. U. S. A. 105, 19336–
707           19341. doi:10.1073/pnas.0810021105

708   Piao, S., Friedlingstein, P., Ciais, P., Viovy, N., Demarty, J., 2007. Growing season extension
709           and its impact on terrestrial carbon cycle in the Northern Hemisphere over the past 2
710           decades. Global Biogeochem. Cycles 21, 1–11. doi:10.1029/2006GB002888

711   Privette, J.L., Eck, T.F., Deering, D.W., 1997. Estimating spectral albedo and nadir reflectance
712           through inversion of simple BRDF models with AVHRR/MODIS-Iike data. J. Geophys.
713           Res. 102, 29529–29542.

714   Richardson, A.D., Anderson, R.S., Arain, M.A., Barr, A.G., Bohrer, G., Chen, G., Chen, J.M.,
715           Ciais, P., Davis, K.J., Desai, A.R., Dietze, M.C., Dragoni, D., Garrity, S.R., Gough, C.M.,
716           Grant, R., Hollinger, D.Y., Margolis, H. a., McCaughey, H., Migliavacca, M., Monson,
717           R.K., Munger, J.W., Poulter, B., Raczka, B.M., Ricciuto, D.M., Sahoo, A.K., Schaefer, K.,
718           Tian, H., Vargas, R., Verbeeck, H., Xiao, J., Xue, Y., 2012. Terrestrial biosphere models
719           need better representation of vegetation phenology: results from the North American
720           Carbon Program Site Synthesis. Glob. Chang. Biol. 18, 566–584. doi:10.1111/j.1365-
721           2486.2011.02562.x

722   Richardson, A.D., Hollinger, D.Y., Dail, D.B., Lee, J.T., Munger, J.W., O'keefe, J., 2009.
723           Influence of spring phenology on seasonal and annual carbon balance in two contrasting
724           New England forests. Tree Physiol. 29, 321–331.

725   Richardson, A.D., Keenan, T.F., Migliavacca, M., Ryu, Y., Sonnentag, O., Toomey, M., 2013.
726           Climate change, phenology, and phenological control of vegetation feedbacks to the climate
727           system. Agric. For. Meteorol. 169, 156–173. doi:10.1016/j.agrformet.2012.09.012

728   Richardson, A.D., O'Keefe, J., 2009. Phenological differences between understory and overstory
729           a case study using the long-term Harvard Forest records, in: Phenology of Ecosystem
730           Processes: Applications in Global Change Research. pp. 87–117. doi:10.1007/978-1-4419-
731           0026-5_4

732   Román, M.O., Schaaf, C.B., Lewis, P., Gao, F., Anderson, G.P., Privette, J.L., Strahler, A.H.,
733           Woodcock, C.E., Barnsley, M., 2010. Assessing the coupling between surface albedo
734           derived from MODIS and the fraction of diffuse skylight over spatially-characterized
735           landscapes. Remote Sens. Environ. 114, 738–760. doi:10.1016/j.rse.2009.11.014

736     Román, M.O., Schaaf, C.B., Woodcock, C.E., Strahler, A.H., Yang, X., Braswell, R.H., Curtis,
737        P.S., Davis, K.J., Dragoni, D., Goulden, M.L., 2009. The MODIS (Collection V005)
738        BRDF/albedo product: Assessment of spatial representativeness over forested landscapes.
739        Remote Sens. Environ. 113, 2476–2498. doi:10.1016/j.rse.2009.07.009

740     Roy, D.P., Ju, J., Lewis, P., Schaaf, C., Gao, F., Hansen, M., Lindquist, E., 2008. Multi-temporal
741        MODIS–Landsat data fusion for relative radiometric normalization, gap filling, and
742        prediction of Landsat data. Remote Sens. Environ. 112, 3112–3130.
743        doi:10.1016/j.rse.2008.03.009

744     Running, S.W., Baldocchi, D.D., Turner, D.P., Gower, S.T., Bakwin, P.S., Hibbard, K.A., 1999.
745        A Global Terrestrial Monitoring Network Integrating Tower Fluxes, Flask Sampling,
746        Ecosystem Modeling and EOS Satellite Data. Remote Sens. Environ. 70, 108–127.
747        doi:10.1016/S0034-4257(99)00061-9

748     Sanchez-Mejia, Z.M., Papuga, S.A., 2014. Observations of a two-layer soil moisture influence
749        on surface energy dynamics and planetary boundary layer characteristics in a semiarid
750        shrubland. Water Resour. Res. 50, 306–317. doi:10.1002/2013WR014135

751     Sanchez-Mejia, Z.M., Papuga, S.A., Swetish, J.B., Van Leeuwen, W.J.D., Szutu, D., Hartfield,
752        K., 2014. Quantifying the influence of deep soil moisture on ecosystem albedo: The role of
753        vegetation. Water Resour. Res. 50, 4038–4053. doi:10.1002/2013WR014150

754     Schaaf, C.B., 2008. Albedo and Reflectance Anisotropy, Terrestrial Essential Climate Variables
755        for Climate Change Assessment, Mitigation and Adaptation, in: Sessa, R., Han, D. (Eds.),
756        GTOS-52. pp. 28–29.

757     Schaaf, C.B., Gao, F., Strahler, A.H., Lucht, W., Li, X., Tsang, T., Strugnell, N.C., Zhang, X.,
758        Jin, Y., Muller, J.-P., Lewis, P., Barnsley, M., Hobson, P., Disney, M., Roberts, G.,
759        Dunderdale, M., Doll, C., d'Entremont, R.P., Hu, B., Liang, S., Privette, J.L., Roy, D.,
760        2002. First operational BRDF, albedo nadir reflectance products from MODIS. Remote
761        Sens. Environ. 83, 135–148. doi:10.1016/S0034-4257(02)00091-3

762     Schaaf, C.B., Liu, J., Gao, F., Strahler, A.H., 2011. MODIS Albedo and Reflectance Anisotropy
763        Products from Aqua and Terra, in: B. Ramachandran, C. Justice, M.A. (Ed.), Land Remote
764        Sensing and Global Environmental Change Remote Sensing and Digital Image Processing.
765        Springer, pp. 549–561.

766     Schimel, D., Hargrove, W., Hoffman, F., MacMahon, J., 2007. NEON: a hierarchically designed
767        national ecological network. Front. Ecol. Environ. 5, 59–59. doi:10.1890/1540-
768        9295(2007)5[59:NAHDNE]2.0.CO;2

769     Sellers, P.J., Meeson, B.W., Hall, F.G., Asrar, G., Murphy, R.E., Schiffer, R. a., Bretherton, F.P.,
770        Dickinson, R.E., Ellingson, R.G., Field, C.B., Huemmrich, K.F., Justice, C.O., Melack,
771        J.M., Roulet, N.T., Schimel, D.S., Try, P.D., 1995. Remote sensing of the land surface for
772        studies of global change: Models — algorithms — experiments. Remote Sens. Environ. 51,
773        3–26. doi:10.1016/0034-4257(94)00061-Q

774     Shuai, Y., Masek, J.G., Gao, F., Schaaf, C.B., 2011. An algorithm for the retrieval of 30-m
775        snow-free albedo from Landsat surface reflectance and MODIS BRDF. Remote Sens.
776        Environ. 115, 2204–2216. doi:10.1016/j.rse.2011.04.019

777     Shuai, Y., Masek, J.G., Gao, F., Schaaf, C.B., He, T., 2014. An approach for the long-term 30-m

778　　　land surface snow-free albedo retrieval from historic Landsat surface reflectance and
779　　　MODIS-based a priori anisotropy knowledge. Remote Sens. Environ. 152, 467–479.
780　　　doi:10.1016/j.rse.2014.07.009

781　Shuai, Y., Schaaf, C., Zhang, X., Strahler, A., Roy, D., Morisette, J., Wang, Z., Nightingale, J.,
782　　　Nickeson, J., Richardson, A.D., Xie, D., Wang, J., Li, X., Strabala, K., Davies, J.E., 2013.
783　　　Daily MODIS 500 m reflectance anisotropy direct broadcast (DB) products for monitoring
784　　　vegetation phenology dynamics. Int. J. Remote Sens. 34, 5997–6016.
785　　　doi:10.1080/01431161.2013.803169

786　Vitasse, Y., Delzon, S., Dufr??ne, E., Pontailler, J.Y., Louvet, J.M., Kremer, A., Michalet, R.,
787　　　2009. Leaf phenology sensitivity to temperature in European trees: Do within-species
788　　　populations exhibit similar responses? Agric. For. Meteorol. 149, 735–744.
789　　　doi:10.1016/j.agrformet.2008.10.019

790　Wang, Z., Schaaf, C.B., Chopping, M.J., Strahler, A.H., Wang, J., Román, M.O., Rocha, A. V.,
791　　　Woodcock, C.E., Shuai, Y., 2012. Evaluation of Moderate-resolution Imaging
792　　　Spectroradiometer (MODIS) snow albedo product (MCD43A) over tundra. Remote Sens.
793　　　Environ. 117, 264–280. doi:10.1016/j.rse.2011.10.002

794　Wang, Z., Schaaf, C.B., Strahler, A.H., Chopping, M.J., Rom??n, M.O., Shuai, Y., Woodcock,
795　　　C.E., Hollinger, D.Y., Fitzjarrald, D.R., 2014. Evaluation of MODIS albedo product
796　　　(MCD43A) over grassland, agriculture and forest surface types during dormant and snow-
797　　　covered periods. Remote Sens. Environ. 140, 60–77. doi:10.1016/j.rse.2013.08.025

798　Woodcock, C.E., Strahler, A.H., Jupp, D.L.B., 1988a. The use of variograms in remote sensing:
799　　　I. Scene models and simulated images. Remote Sens. Environ. 25, 323–348.
800　　　doi:10.1016/0034-4257(88)90108-3

801　Woodcock, C.E., Strahler, A.H., Jupp, D.L.B., 1988b. The use of variograms in remote sensing:
802　　　II. Real digital images. Remote Sens. Environ. 25, 349–379. doi:10.1016/0034-
803　　　4257(88)90109-5

804　Zhang, X., Friedl, M. a., Schaaf, C.B., Strahler, A.H., Hodges, J.C.F., Gao, F., Reed, B.C.,
805　　　Huete, A., 2003. Monitoring vegetation phenology using MODIS. Remote Sens. Environ.
806　　　84, 471–475. doi:10.1016/S0034-4257(02)00135-9

807　Zhang, X., Friedl, M.A., Schaaf, C.B., 2006. Global vegetation phenology from Moderate
808　　　Resolution Imaging Spectroradiometer (MODIS): Evaluation of global patterns and
809　　　comparison with in situ measurements. J. Geophys. Res. G Biogeosciences 111.
810　　　doi:10.1029/2006JG000217

811　Zhang, X., Wang, J., Gao, F., Liu, Y., Schaaf, C., Friedl, M., Yu, Y., Jayavelu, S., Gray, J., Liu,
812　　　L., Yan, D., Henebry, G.M., 2017. Exploration of scaling effects on coarse resolution land
813　　　surface phenology. Remote Sens. Environ. 190, 318–330. doi:10.1016/j.rse.2017.01.001

814　Zhu, X., Chen, J., Gao, F., Chen, X., Masek, J.G., 2010. An enhanced spatial and temporal
815　　　adaptive reflectance fusion model for complex heterogeneous regions. Remote Sens.
816　　　Environ. 114, 2610–2623. doi:10.1016/j.rse.2010.05.032

817　Zurita-Milla, R., Kaiser, G., Clevers, J.G.P.W., Schneider, W., Schaepman, M.E., 2009.
818　　　Downscaling time series of MERIS full resolution data to monitor vegetation seasonal
819　　　dynamics. Remote Sens. Environ. 113, 1874–1885. doi:10.1016/j.rse.2009.04.011

820